Lawrence Berkeley National Laboratory
Recent Work

Title
PbS nanoparticles capped with tetrathiafulvalenetetracarboxylate: utilizing energy level alignment for efficient carrier transport.

Permalink
https://escholarship.org/uc/item/2m68v6zm

Journal
ACS nano, 8(3)

ISSN
1936-0851

Authors
Scheele, Marcus
Hanifi, David
Zherebetskyy, Danylo
et al.

Publication Date
2014-03-01

DOI
10.1021/nn406127s

Peer reviewed

eScholarship.org Powered by the California Digital Library
University of California

PbS Nanoparticles Capped with Tetrathiafulvalenetetracarboxylate: Utilizing Energy Level Alignment for Efficient Carrier Transport

Marcus Scheele,[†,‡] David Hanifi,[§] Danylo Zherebetskyy,[†] Slim T. Chourou,[⊥] Stephanus Axnanda,[∥] Benjamin J. Rancatore,[†,‡] Kari Thorkelsson,[#] Ting Xu,[†,‡,#] Zhi Liu,[∥] Lin-Wang Wang,[†] Yi Liu,[§] and A. Paul Alivisatos[†,‡,*]

[†]Material Sciences Division, Lawrence Berkeley National Laboratory, Berkeley, California 94720, United States, [‡]Department of Chemistry, University of California, Berkeley, California 94720, United States, [§]Molecular Foundry, Lawrence Berkeley National Laboratory, Berkeley, California 94720, United States, [⊥]Computational Research Division, Lawrence Berkeley National Laboratory, Berkeley, California 94720, United States, [∥]Advanced Light Source, Lawrence Berkeley National Laboratory, Berkeley, California 94720, United States, and [#]Department of Materials Science and Engineering, University of California, Berkeley, California 94720, United States

ABSTRACT We fabricate a field-effect transistor by covalently functionalizing PbS nanoparticles with tetrathiafulvalenetetracarboxylate. Following experimental results from cyclic voltammetry and ambient-pressure X-ray photoelectron spectroscopy, we postulate a near-resonant alignment of the PbS $1S_h$ state and the organic HOMO, which is confirmed by atomistic calculations. Considering the large width of interparticle spacing, we observe an abnormally high field-effect hole mobility, which we attribute to the postulated resonance. In contrast to nanoparticle devices coupled through common short-chained ligands, our system maintains a large degree of macroscopic order as revealed by X-ray scattering. This provides a different approach to the design of hybrid organic−inorganic nanomaterials, circumvents the problem of phase segregation, and holds for versatile ways to design ordered, coupled nanoparticle thin films.

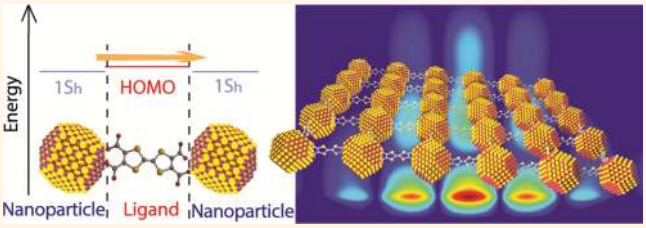

KEYWORDS: semiconductor nanoparticles · organic semiconductors · hybrid materials · field-effect transistors

Hybrid organic−inorganic nanostructures combine the chemical versatility of organic semiconductors with the chemical stability and size-tunable band gaps of inorganic nanomaterials.[1] Their outstanding optoelectronic properties have led to a variety of promising examples for renewable energy applications such as photovoltaic and thermoelectric power generation.[2−5] For the most part, hybrid organic−inorganic nanostructures have been prepared conveniently by mixing the organic and inorganic constituents in a suitable solvent after which they may be solution-processed to a thin film.[6] The disadvantage of this procedure is the inherent tendency of phase segregation between the organic and inorganic moieties, which leads to ill-defined interfaces and inefficient organic−inorganic coupling.[7] In order to fully exploit the potential for resonant alignment between suitable energy levels in the two phases, a promising strategy is functionalization of the organic part with a coordinating group capable of directly binding to the surface of the inorganic nanostructure. For this inorganic−organic core−shell structure, a remarkable enhancement in energy transfer and the luminescence stability is observed in comparison to a blended version of the same material.[8] Typically, such core−shell structures have been fabricated with dendronized polymers, many of which were based on oligothiophenes.[9−11] However, the large size of these molecules can become highly detrimental to in-film charge carrier transport, and, consequently, most studies focused on the optical properties of these hybrid structures. In contrast, tetrathiafulvalene (TTF) is a rather small and simple organic semiconductor that has been studied extensively.[12−19] Functionalization of TTF with

* Address correspondence to alivis@berkeley.edu.

Received for review November 27, 2013 and accepted February 13, 2014.

Published online February 13, 2014
10.1021/nn406127s

© 2014 American Chemical Society

coordinating end groups is readily afforded and provides the basis for its rich and versatile chemistry.[20,21] Particularly suitable as a building block in more complex molecular structures is the tetracarboxylate derivative ($TTFTA^{4-}$) due to its relatively facile synthesis and robustness toward air.[22,23] As such, $TTFTA^{4-}$ has been applied as a coordinating ligand in metal complexes and 3D-coordination polymers.[24−26] In terms of conjugates of inorganic nanoparticles and derivatives of TTF, we note two studies of TTF−tetrathiolate cross-linked CdSe and Au nanocrystals.[27,28] Despite a remarkable redox stability and the occurrence of additional optical features that could be interpreted with ligand-mediated coupling, the electric properties of these conjugates have not been investigated. For this purpose, PbS nanoparticles bear significant advantages due to their small carrier effective masses (0.09 m_0), high static dielectric constant, and large exciton Bohr radius (18 nm).[29−31] The combination of large carrier mobilities and extraordinary tunability of energy levels provided by these properties allows for the rational study of electronic coupling between nanoparticle and ligand as a function of energy level offsets.

In this work, we study electric transport through a thin film of PbS nanoparticles cross-linked with $TTFTA^{4-}$. Starting with ordered, self-assembled films of PbS nanocrystals (NC) capped with $Pb[Oleate]_2$ we perform a ligand exchange with $TTFTA^{4-}$ to fabricate thin films of PbS-TTFTA core−shell semiconductor nanoparticles. We show that the initial in-film order is largely preserved on exchange with $TTFTA^{4-}$, which is generally not afforded by previous protocols applying shorter ligands.[32−37] Using field-effect transistor measurements, we find an unusually large mobility in comparison to nonconjugated ligands of similar length. Utilizing cyclic voltammetry (CV) and ambient pressure X-ray photoelectron spectroscopy (AP-XPS), together with theoretical multistep calculations, we construct an energy level diagram to explain this behavior with a near-resonant alignment of the $1S_h$ state in PbS NCs and the highest occupied molecular orbital (HOMO) in $TTFTA^{4-}$. The measured mobility of 2×10^{-3} $cm^2/(V\,s)$ demonstrates the feasibility to modify transport in a hybrid organic−inorganic system through the design of a well-defined interface and by utilizing suitable energy levels provided by the cross-linking ligand.

RESULTS

PbS nanocrystals of 9.8 nm capped with $Pb[Oleate]_2$ are synthesized following the procedure established by Hines *et al.*[38] The optical properties with a ground-state excitation ($\Delta 1S_e \leftarrow 1S_h$) of 0.59 eV and transmission electron microscopy (TEM) images are displayed in Figure 1.

To determine the energy of the $1S_h$ state, we use ambient-pressure X-ray photoelectron spectroscopy following a previously developed procedure.[39] The advantage of this technique is the ability to determine the Fermi level (E_F) of a nanoparticle ensemble with high accuracy (±0.1 eV) and under device testing conditions, that is, near atmospheric pressure, which is not afforded by comparable techniques such as cyclic voltammetry or ultraviolet photoelectron spectroscopy. By tracking the binding energy of the argon 2p core levels in the vicinity of the sample, we locate E_F at −4.95 eV *vs* vacuum. We apply an effective medium approach to determine the effective density of states (N_H) and use the hole concentration (n_h) extracted by field-effect transistor measurements to obtain the energy of the $1S_h$ state according to

$$E_F - E(1S_h) = kT \ln\left(\frac{N_H}{n_h}\right)$$

at −5.13 eV *vs* vacuum. For details of this method, the reader is referred to the SI.

The tetrabutylammonium (TBA) cation is chosen as the counterion for the $TTFTA^{4-}$ ligand as (1) TBA is chemically inert and thus noninvasive to the quantum dots and (2) it can alter the solubility of the ligands to be more compatible with the PbS quantum dots. $[TBA]_4TTFTA$ is synthesized by slightly modifying a previously reported protocol and is shown to be very soluble in common organic solvents such as chloroform and acetonitrile.[22,23] Using cyclic voltammetry, we find two one-electron redox couples, centered about −4.64 and −4.96 eV *vs* vacuum, respectively, which correspond to the stepwise formation of a radical cation and dication, stabilized by the gain in heteroaromaticity (see Figure 2a). Qin *et al.* have reported redox couples of −4.91 and −5.28 eV *vs* vacuum for Na_4TTFTA.[23] While the energy difference between the two species is in good agreement with our measurement, we attribute the offset in absolute energy to the different measurement conditions (this work: in solution with glassy carbon; Qin *et al.*: solid state with surface-modified platinum electrode). In view of an earlier work by Mercier *et al.* on the neutral tetraacid (−5.06 eV) and the partially deprotonated dianion (−4.97 eV) the results also follow the expected trend to an electron-richer compound as the acid is fully deprotonated.[40]

UV−vis spectroscopy in acetonitrile reveals bands at 2.7, 3.2, 3.8, and 4.2 eV and a broad feature at 4.6−5.3 eV. Adapting the assignment following theoretical considerations for the similar compound dimethylthio-TTF monocarboxylic acid by Zhu *et al.*, we assign the first four bands to the LUMO (lowest unoccupied molecular orbital) ← HOMO, LUMO+2 ← HOMO, LUMO ← HOMO−1, and LUMO+1 ← HOMO−1 transitions.[41] The tailing toward lower energies near the LUMO ← HOMO transition indicates a small amount of the dianionic species $[TTF(CO_2H)_2(CO_2)_2]^{2-}$, which has an additional transition at 2.3 eV.[40] This species is readily obtained upon exposing $TTFTA^{4-}$ to water, as verified

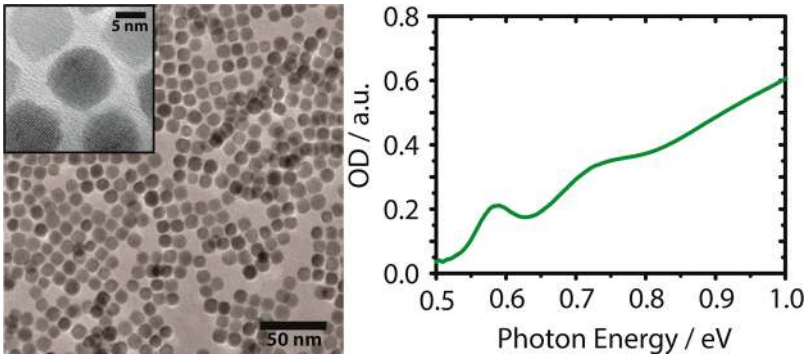

Figure 1. (Left) Transmission electron microscopy images of 9.8 nm PbS nanoparticles used in this study. (Right) Absorption spectrum in solution of the PbS nanoparticle samples capped with Pb[Oleate]$_2$.

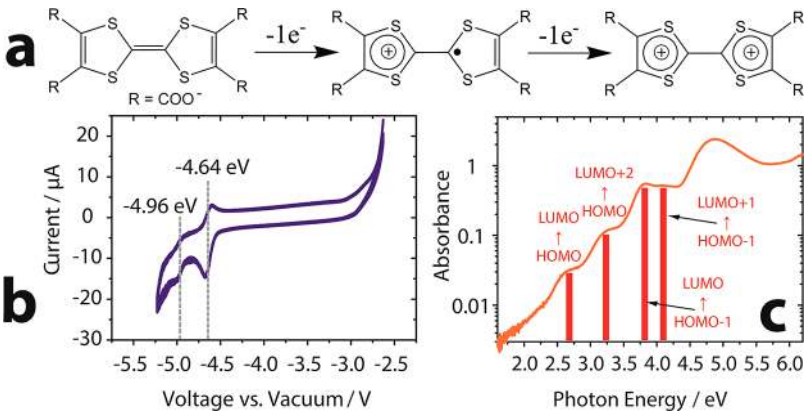

Figure 2. (a) The two one-electron oxidation processes associated with tetrathiafulvelene derivatives. (b) Cyclic voltammetry of tetrabutylammonium tetrathiafulvalenetetracarboxylate ([TBA]$_4$TTFTA) in acetontitrile. The two dashed lines mark the two oxidative one-electron processes and the corresponding potentials relative to the absolute vacuum level. (c) Absorption spectrum of [TBA]$_4$TTFTA in acetonitrile. Solid lines mark individual bands that are assigned by adapting previous theoretical predictions.[41]

by single-crystal X-ray diffraction and electrospray ionization mass spectroscopy (see SI for details) and leads to a bright red color. Upon titration with a base, the partial protonation is reversed, the transition at 2.3 eV vanishes as indicated by a color change to yellow, and TTFTA^{4-} is restored.

Using the combined spectroscopic and electrochemical information, we compare the energy of the 1S$_h$ and 1S$_e$ state in 9.8 nm PbS nanoparticles with the energy of relevant molecular orbitals in TTFTA^{4-} in Figure 3a. The 1S$_h$ energy is obtained from AP-XPS and the HOMO of TTFTA^{4-} from CV as described above. The locations of the PbS 1S$_e$ level and the TTFTA^{4-} LUMO are calculated by adding the optical energy gap to the energy of the 1S$_h$ state and the HOMO, respectively. The HOMO of the easily formed TTFTA$^{3-\bullet}$ is inferred from the second redox wave in the CV measurement and displayed as well. The remaining orbitals are calculated from the additional bands in the UV/vis spectrum. We stress that this comparison does not take into account any electrochemical effects on the TTFTA^{4-} orbitals upon functionalizing the particles' surface.

To investigate these effects in greater detail, we have performed theoretical calculations using density functional theory with the hybrid Heyd–Scuseria–Ernzerhof (HSE03) functional, the GW method, and the projector augmented wave (PAW) pseudopotentials as implemented in the VASP software package.[42−46] TTF(CO$_2$H)$_4$ is attached to the PbS {001} facet, and the band alignment between the ligand in its neutral, fully protonated form and bulk PbS is first calculated using a PbS slab. The result (after removing the slab quantum confinement effect) is shown as HSE03 in Figure 3b. After adding a spin–orbit effect to the PbS energy levels we obtain the expected bulk energy gap of 0.31 eV. The bulk and isolated molecule GW quasiparticle correction is added on top of the HSE03 results followed by a correction for the quantum confinement effect to the PbS 1S$_h$ and 1S$_e$ levels.[47] Finally, a long-range polarization effect due to the QD surface is added based on the linear-scaling three-dimensional fragment (LS3DF) method.[48−50] All these effects are based on atomistic calculations. The details are provided in the SI. It is apparent that these corrections have significantly changed the initial HSE03 band alignment, especially applying the GW approximation to the TTFTA system.

To fabricate a thin film of PbS-TTFTA, we apply a two-step procedure. First, we deposit a film of PbS

nanocrystals capped with Pb[Oleate]$_2$ onto a substrate of choice, which is in turn exchanged by a solution of [TBA]$_4$TTFTA in acetonitrile. In Figure 4, we present the Fourier transformed infrared (FT-IR) signal before and after this procedure. The complete disappearance of C−H vibrations (around 3000 cm^{-1}) is indicative of a near-complete removal of the native Pb[Oleate]$_2$ ligand and the role of TBA as a mere spectator ion, which is replaced by Pb^{2+} during the exchange. The chemical nature of the surface before and after exchange is further studied by XPS. Figure 4d and e show spectra in the S-2p core region of the [TBA]$_4$TTFTA-treated PbS particles and of the same particles before ligand exchange, respectively. We attribute the new, additional sulfur species between 163 and 166 eV to the sulfur atoms in TTFTA^{4-}.

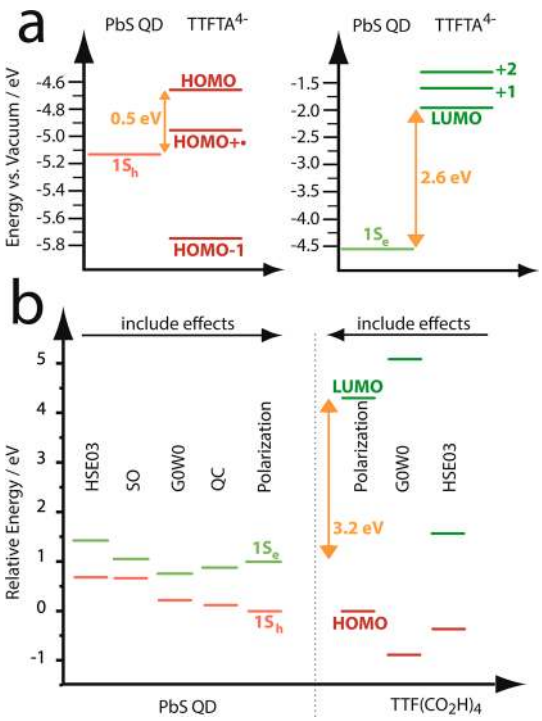

Figure 3. (a) Comparison of energy levels for PbS nanoparticles and free TTFTA^{4-} derived by experiment. The left graph displays the region near the 1S$_h$ state, whereas the right side represents the 1S$_e$ region. (b) Calculated energy levels of a 9.8 nm PbS nanoparticle (left) and a covalently bound TTF(CO$_2$H)$_4$ molecule (right). The final results are the offsets next to the dashed line, which are obtained by starting with a basic Heyd−Scuseria−Ernzerhof functional (HSE03) and consecutively taking into account spin−orbit (SO) effects, the GW approximation (G0W0), quantum confinement (QC), and polarization effects wherever applicable.

In Figure 5, we study the effect of ligand exchange with [TBA]$_4$TTFTA onto the short- and long-range order in as-deposited films of Pb[Oleate]$_2$-capped 9.8 nm PbS particles. After ligand exchange, the fast Fourier transformation (FFT) of a low-magnification scanning electron microscopy (SEM) image (Figure 5a; for the original image see the SI) contains a large number of frequencies of similar lattice spacings and similar, but slightly tilted crystalline orientations. This indicates poor long-range order but a high degree of short-range order. The TEM image in Figure 5b reveals the reduced interparticle spacing and preferred crystalline orientation upon exchange with [TBA]$_4$TTFTA: the TTFTA^{4-} ion is approximately 9.6 Å in length. The average interparticle spacing in the TEM image is 10 ± 3 Å with most particles facing their nearest neighbors *via* the {100} facet. From this, we conclude that PbS nanoparticles are cross-linked by a monolayer of [Pb]$_2$TTFTA bound to their {100} facets.

These results are further verified by grazing incidence small-angle X-ray scattering (GISAXS). Using the HipGISAXS software package we seek to validate the nanoparticle shape and its spatial distribution by fitting the computed GISAXS pattern to the experimental images given in Figure 5d and f.[51] Our simulation is carried out by modeling the PbS nanoparticle film as a collection of rhombicuboctahedral PbS nanoparticles 9.8 nm in size positioned to face their {100} facets in a 10 nm layer. Where further details to this simulation are given in the SI, an overall agreement is observed in terms of the positions, relative intensity, and shape of the peaks. Consistent with previous reports, the GISAXS pattern of Pb[Oleate]$_2$-capped films indicates a high degree of long-range order.[52] We obtain reasonable aggreement between simulation and experiment

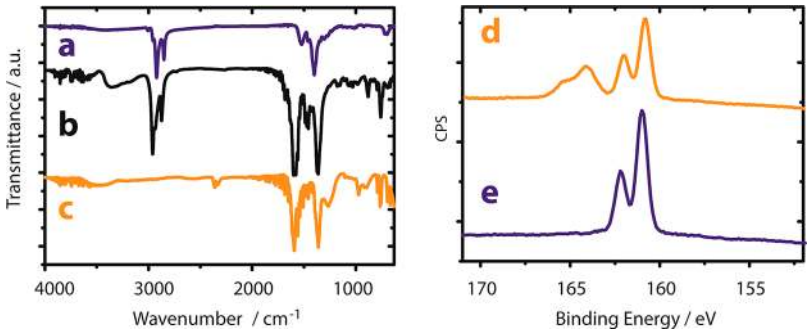

Figure 4. Fourier transformed infrared (FT-IR) and X-ray photoelectron spectra (XPS) in the S-2p core region of individual components of PbS-TTFTA hybrid organic−inorganic nanoparticles. (a) FT-IR of PbS-Oleate, (b) FT-IR of [TBA]$_4$TTFTA, (c) FT-IR of PbS-TTFTA, (d) XPS of PbS-TTFTA, and (e) XPS of PbS-Oleate.

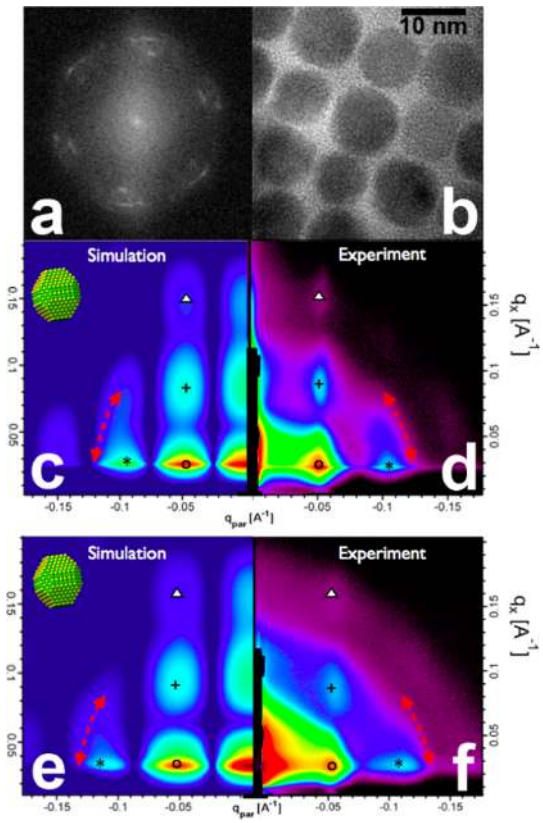

Figure 5. (a) Fast Fourier transformation of a low-magnification SEM image of a PbS-TTFTA nanoparticle thin film. The original image is provided in the SI. (b) Transmission electron microscopy (TEM) image of self-assembled PbS-TTFTA nanoparticles. (c−f) Simulation and experimental GISAXS images (left and right panel, respectively) for PbS-Oleate (c, d) and PbS-TTFTA (e, f) thin films. Corresponding peaks are indicated by the same symbol.

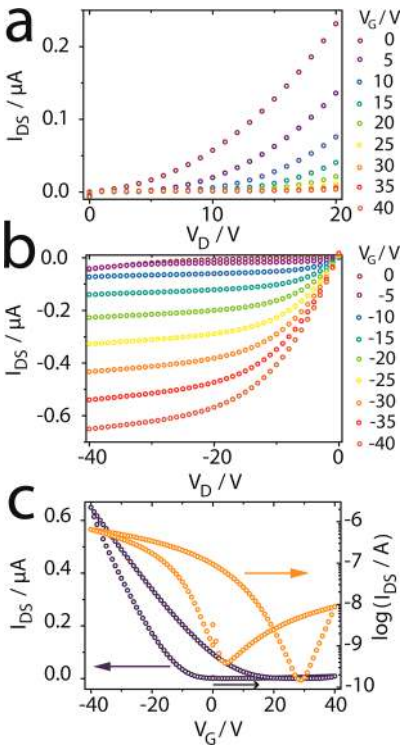

Figure 6. Field-effect transistor characteristics of thin films of 9.8 nm PbS-TTFTA. (a, b) Positive and negative source−drain sweeps, with the applied gate voltages for an individual sweep denoted next to each color. (c) Transconductance under a constant bias of +5 V. Left and right axes are linear and logarithmic plots of the same measurement, respectively. The black arrow indicates the beginning and direction of the closed loop scan.

with a lattice constant of 12.7 ± 0.1 nm in a cubic lattice with average dimensions of 500 nm × 500 nm. The shape of the peaks validates the assumption of rhombicuboctahedral nanoparticles as indicated by the segmented ring pattern. After ligand exchange with $TTFTA^{4-}$, the GISAXS pattern is largely preserved, which is generally not afforded by other ligand exchange procedures.[32,53,54] The peaks' positions and relative intensity support the organization of the nanoparticles in a small cubic lattice (roughly 100 nm × 100 nm) with a lattice constant of 10.5 ± 0.3 nm.

In Figure 6, we study electric transport in assembled $[Pb]_2$TTFTA-capped PbS nanoparticle films by field-effect transistor (FET) measurements and display the positive (a) and negative (b) drain voltage sweeps as well as the transconductance (c). We find p-type behavior with field-effect mobilities in the linear regime of 2.0×10^{-3} $cm^2/(V\ s)$ and a hole concentration of 6×10^{15} cm^{-3}.

DISCUSSION

We choose AP-XPS over CV to measure the absolute energy of the $1S_h$ state in PbS nanoparticles to avoid the inherent challenges associated with the latter method due to surface defects, dangling bonds, and surface inhomogeneities. Photoelectron spectroscopy (PES) has been applied before by other groups to measure the size-dependent $1S_h$ position on lead chalcogenide nanoparticles.[55,56] Typically, the $1S_h$ state is found to be remarkably insensitive to size variations, which is attributed to either a large effective mass of holes or Fermi level pinning.[56,57] Given the similar hole and electron mobilities found in films of PbS nanocrystals, the former seems unlikely, which leaves Fermi level pinning as the main disadvantage of PES-based determinations of the $1S_h$ state. With AP-XPS, the position of the Fermi level is measured directly, and pinning effects may conveniently be tracked. We find a depression of E_F of 140 meV when changing the PbS diameter from 9.8 nm to 2.9 nm, which shows that Fermi level pinning is at least partially suppressed by our measurement conditions. The position of the $1S_h$ state of 9.8 nm PbS-TTFTA particles (−5.13 eV) used in this work is 280 meV lower than predicted for PbS-Oleate nanocrystals and 230 meV lower for PbS capped with mercaptopropionic acid of the same diameter.[55,58] This discrepancy may be explained by the change in electrochemical environment provided by the different ligands.[39,55]

The experimentally derived (a) and calculated (b) energy level diagrams in Figure 3 are overall in good agreement and describe the selective electronic coupling in PbS-TTFTA nanoparticles. The potential barrier for electron transport (2.6/3.2 eV) is seen to be much larger than the barrier to hole transport (0.5/0.0 eV). In light of the subtle discrepancies between experiment and calculation, we note a few important differences:

(1) The experimentally derived MOs of $TTFTA^{4-}$ resemble those of the pure compound without the interaction of the PbS nanoparticle surface. In contrast, our calculation takes this effect into account upon applying the GW approximation.

(2) Optical spectroscopy underestimates the HOMO−LUMO gap by the excitonic binding energy. For a wide-gap organic semiconductor, this difference can be as much as 1 eV. In the GW approximation, this term is excluded.

(3) Since electron microscopy suggests that adjacent nanoparticles are cross-linked with $TTFTA^{4-}$ *via* the neutral {001} facet, the electron counting rule forces us to operate with the neutral, fully protonated acid $TTF(CO_2H)_4$ in calculations. The experimentally determined HOMO, however, is that of the fully deprotonated $TTFTA^{4-}$. The energy difference between the two HOMOs is about 0.4 eV, which accounts for the majority of the discrepancy between our experimental and theoretical results.[40]

The electronic structure of $TTFTA^{4-}$ holds for a second possible pathway for hole transport in PbS-TTFTA: The experimentally derived HOMO of the $TTFTA^{3-\bullet}$ radical is in even closer proximity (0.15 eV) to the $1S_h$ state of 9.8 nm PbS nanoparticles. Although carboxylic acids of TTF are generally quite stable, chemical oxidation to the aromatic radicals (see also Figure 2a) has recently been demonstrated.[41] Since PbS nanoparticles are inherently p-type, empty states appropriate for electron transfer from $TTFTA^{4-}$ to PbS should be available and the $TTFTA^{3-\bullet}$ radical could be formed.

We note that the various degrees of freedom of the TTFTA system in terms of redox state and degree of protonation hold for challenges but also versatility in terms of controlling electronic coupling to PbS nanoparticles. The decrease of the HOMO−LUMO gap upon exposure to moisture and formation of $[TTF(CO_2H)_2(CO_2)_2]^{2-}$ is highlighted again in this respect. This molecule hosts two rigid seven-membered rings held together *via* almost symmetric hydrogen bonding and an abnormally short O···O distance of 2.387 Å, similar to hydrogen maleate.[59] This extraordinary stability not only manifests in a smaller energy gap but also significantly reduces the binding affinity toward the PbS surface. We find that only the fully deprotonated $TTFTA^{4-}$ leads to the FT-IR characteristics displayed in Figure 4a, whereas the dianionic species results in visibly incomplete removal of the native oleate ligand (see SI).

If the size dispersion of a colloidal nanoparticle sample is sufficiently narrow, crystal-like long-range order in nanoparticle films may be achieved.[60] When an ordered film of nanoparticles capped with $Pb[Oleate]_2$ is treated with a short-chained ligand such as Pb[ethanedithiolate], hydrazine, pyridine, or methylamine, strain is imposed onto the superlattice of nanoparticles due to the length difference between the old and new ligand, which leads to the complete destruction of the superlattice.[32,53,54] Because $[Pb]_2TTFTA$ is rigid and significantly longer than the above-mentioned examples (10 vs 3−5 Å), the imposed strain on exchange from $Pb[Oleate]_2$ is small and isolated domains (typically about 100 nm × 100 nm in area) with preserved ordering are obtained (Figure 5). In addition, Wang *et al.* have recently shown that arrays of PbS nanoparticles undergo a phase transition from amorphous/short-range ordered to crystalline/long-range ordered supercrystals when the interparticle spacing is 1.8 nm or larger.[61] For $Pb[Oleate]_2$ capping of 9.8 nm PbS nanoparticles, we obtain a GISAXS-derived interparticle spacing of 2.9 ± 0.1 nm, while for $[Pb]_2TTFTA$ capping, the spacing is 0.7 ± 0.3 nm. This is consistent with the different degrees of ordering observed for the two materials and also supports the view that the particles are separated by just one monolayer of $[Pb]_2TTFTA$, highlighting its bidentate nature of binding.

As demonstrated in Figure 6, transport in films of 9.8 nm PbS-TTFTA is p-type with a weak contribution by electrons. We attribute this to the large energetic difference between $E(HOMO) - E(1S_h)$ and $E(LUMO) - E(1S_e)$, which greatly favors hole transport. The transconductance scan (Figure 6c) reveals a visible preference for hole over electron transport, but hysteresis on the return scan—most likely due to electron trapping and typical for lead chalcogenide transistors—does not allow for a quantitative derivation of the electron mobilities.[62] For comparison, we functionalized the same nanoparticles with 1,9-nonanedithiol. Although the nominal length of this ligand is about 13 Å, its flexible structure leads to interparticle spacings of ∼10 Å as verified by GISAXS.[63,64] With this surface passivation, no functional devices could be fabricated. Although the different terminal groups could be partially responsible for the altered transport behavior, it is well established for lead chalcogenide solids that the functional group of the linker strongly affects the carrier concentration but hardly the mobility. The latter is dominated by the length of the ligand and has been found to be very similar for dithiols and carboxylic acids of the same chain length.[37,63] Further, Law and co-workers demonstrated that complete surface coverage and saturation of dangling bonds by matrix encapsulation can increase the mobility of lead

chalcogenide NCs by over an order of magnitude.[65] However, it is hard to imagine why such efficient saturation should occur upon TTFTA functionalization, especially since thiols are usually more effective in removing intraband states from PbS nanoparticles than carboxylic acids. This leaves energy level alignment between the $1S_h$ state and HOMO as demonstrated electrochemically and computationally throughout this article as the most likely explanation for the functionality of PbS-TTFTA-based transistors.

CONCLUSION

By functionalizing PbS nanoparticles with tetrathiafulvalenetetracarboxylate ($TTFTA^{4-}$), we have fabricated a homogeneously distributed hybrid organic–inorganic semiconductor nanoparticle thin film. In contrast to previous attempts to decrease the width of the transport barrier, we realize internanoparticle coupling by reducing the barrier height. This is achieved by a near-resonant alignment of the PbS $1S_h$ state and the $TTFTA^{4-}$ HOMO, providing a selective channel for holes at every nanoparticle/ligand interface. The structural rigidity of $TTFTA^{4-}$ allows for the ordered self-assembly into periodic lattices. Such ordered, covalently linked, and carrier-selective hybrid nanomaterials provide great prospects for the design of electric devices where the controlled assembly, discrimination between charge carriers, and persistence to phase segregation are crucial, such as photovoltaics or thermoelectrics.

METHODS

Synthesis of PbS. The PbS quantum dot samples were synthesized by a previously reported method.[38] 90 mg of PbO (Aldrich, >99%) and 4.0 mL of oleic acid (Aldrich, 90%) were heated under vacuum at 100 °C for 2 h, then brought to 150 °C under an argon atmosphere. A solution of 62 μL of trimethylsilylsulfide (Aldrich) in 2 mL of Trioctylphosphine TOP was quickly injected, upon which the temperature was lowered to 120 °C. After 150 s, the reaction was terminated by injecting 10 mL of cold, anhydrous hexanes.

The nanocrystals were precipitated by the addition of anhydrous ethanol, the suspension was centrifuged for 5 min at 4500 rpm, the supernatant was discarded, and the precipitate was dissolved in anhydrous toluene. It was washed two more times on adding anhydrous methanol and one more time with acetone. Finally the nanocrystals were stored in a 9:1 mixture of anhydrous hexanes/octane.

Synthesis of $TTFTA^{4-}$. The neutral TTF tetracarboxylic acid was synthesized as previously described.[25] The tetraacid (60 mg, 0.17 mmol) was suspended in anhydrous MeOH (1 mL), to which tetrabutylammonium hydroxide (4 equiv, 1.0 M solution in MeOH) was added. The resulting mixture was stirred at room temperature for 2 h, followed by filtration to remove the partially deprotonated TTF salts. The volume of the remaining filtrate was concentrated to 0.5 mL. Upon addition of ethyl ether (~100 mL), an oily precipitate was obtained, which was rinsed thoroughly with ether to give tetrabutylammonium-tetrathiafulvalenetetracarboxylate ($[TBA]_4TTFTA$) (192 mg, 85% yield) as an orange semisolid.

Ligand Exchange with $TTFTA^{4-}$. A 3 mg amount of $[TBA]_4TTFTA$ was dissolved with 3 mL of acetonitrile. Substrates for field-effect transistors were cleaned on using a soap scrub and rinsing with distilled water, followed by 2-propanol and then acetone, blow-dried, plasma-cleaned for 5 min, and mounted onto a spin-coater. One drop of a filtered hexanes/octane (9:1) solution of nanoparticles (roughly 10 mg/mL) was drop-cast onto the substrate, allowed to dwell for 5 s, and spun at 2000 rpm with a 1 s ramp for 15 s. At rest, the substrate was covered with the $TTFTA^{4-}$ solution (approximately 200 μL) and allowed to dry completely within roughly 10 min. While spinning at 2000 rpm, it was washed with acetonitrile to spin off excess $TTFTA^{4-}$, followed by hexanes to wash off the oleate. This procedure was repeated until a thickness of roughly 50 nm had been reached as determined from ellipsometry.

Conflict of Interest: The authors declare no competing financial interest.

Supporting Information Available: (S1) AP-XPS measurement and calibration. (S2) SEM image of 9.8 nm PbS nanoparticles capped with $[Pb]_2TTFTA$. (S3, S4) Comparison of different form factors for self-assembled 9.8 nm PbS nanoparticles and the effect on computed GISAXS images. (S5) Absorption spectrum of TTFTA with various degrees of protonation in water. (S6) Chemical, X-ray crystal structure and ESI-MS spectrum of $[TTF(CO_2H)_2(CO_2)_2]^{2-}$. (S7) FT-IR spectra of PbS nanoparticles before and after ligand exchange with $[TTF(CO_2H)_2(CO_2)_2]^{2-}$. (S8) Optimized geometry of $TTF(CO_2H)_4$ molecules on the PbS-(001) surface. (S9) DOS of $TTF(CO_2H)_4$ molecules on the PbS(001) surface. (S10) Atomic structure, total charge density, HOMO and LUMO wave functions of a cuboctahedral PbS nanoparticle. Description of characterization techniques, effective medium approach, GISAXS modeling, and theoretical calculations. This material is available free of charge *via* the Internet at http://pubs.acs.org.

Acknowledgment. The authors gratefully acknowledge financial support by the Self-Assembly of Organic/Inorganic Nanocomposite Materials program (supported by the Office of Science, Office of Basic Energy Sciences, U.S. Department of Energy, under contract DE-AC02-05CH11231) for X-ray scattering and photoelectron spectroscopy experiments. The synthesis of ligands was performed as a User Project at the Molecular Foundry, Lawrence Berkeley National Laboratory, which was supported by the Office of Science, Office of Basic Energy Sciences, U.S. Department of Energy, under contract DE-AC02-05CH11231. Nanoparticle synthesis and characterization, ligand exchange, sample preparation, and transport measurements were funded by the Helios Solar Energy Research Center, which is supported by the Director, Office of Science, Office of Basic Energy Sciences of the U.S. Department of Energy, under contract no. DE-AC02-05CH11231. M.S. would like to thank the Alexander von Humboldt-Foundation for a Feodor Lynen-Fellowship. We thank Jesse Engel for critical review and discussion of the transport results and Dr. Simon Teat of the Advanced Light Source for help with single-crystal X-ray analysis.

REFERENCES AND NOTES

1. Park, Y.; Advincula, R. C. Hybrid Semiconductor Nanoparticles: Pi-Conjugated Ligands and Nanostructured Films. *Chem. Mater.* **2011**, *23*, 4273–4294.
2. Agranovich, V. M.; Gartstein, Y. N.; Litinskaya, M. Hybrid Resonant Organic-Inorganic Nanostructures for Optoelectronic Applications. *Chem. Rev.* **2011**, *111*, 5179–5214.
3. Du, Y.; Shen, S. Z.; Cai, K.; Casey, P. S. Research Progress on Polymer-Inorganic Thermoelectric Nanocomposite Materials. *Prog. Polym. Sci.* **2012**, *37*, 820–841.
4. Huynh, W. U.; Dittmer, J. J.; Alivisatos, A. P. Hybrid Nanorod-Polymer Solar Cells. *Science* **2002**, *295*, 2425–2427.
5. Moule, A. J.; Chang, L.; Thambidurai, C.; Vidu, R.; Stroeve, P. Hybrid Solar Cells: Basic Principles and the Role of Ligands. *J. Mater. Chem.* **2012**, *22*, 2351–2368.

6. Zhang, Q.; Atay, T.; Tischler, J. R.; Bradley, M. S.; Bulovic, V.; Nurmikko, A. V. Highly Efficient Resonant Coupling of Optical Excitations in Hybrid Organic/Inorganic Semiconductor Nanostructures. *Nat. Nanotechnol.* **2007**, *2*, 555–559.
7. Juhl, A.; Busbee, J.; Koval, J.; Natarajan, L.; Tondiglia, V.; Vaia, R.; Bunning, T.; Braun, P. Holographically Directed Assembly of Polymer Nanocomposites. *ACS Nano* **2010**, *4*, 5953–5961.
8. Odoi, M. Y.; Hammer, N. I.; Sill, K.; Emrick, T.; Barnes, M. D. Observation of Enhanced Energy Transfer in Individual Quantum Dot-Oligophenylene Vinylene Nanostructures. *J. Am. Chem. Soc.* **2006**, *128*, 3506–3507.
9. Milliron, D. J.; Alivisatos, A. P.; Pitois, C.; Edder, C.; Fréchet, J. M. J. Electroactive Surfactant Designed to Mediate Electron Transfer between CdSe Nanocrystals and Organic Semiconductors. *Adv. Mater.* **2003**, *15*, 58–61.
10. Stalder, R.; Xie, D.; Zhou, R.; Xue, J.; Reynolds, J. R.; Schanze, K. S. Variable-Gap Conjugated Oligomers Grafted to CdSe Nanocrystals. *Chem. Mater.* **2012**, *24*, 3143–3152.
11. Zhang, Y.; Chen, Y.; Niu, H.; Gao, M. Formation of CdS Nanoparticle Necklaces with Functionalized Dendronized Polymers. *Small* **2006**, *2*, 1314–1319.
12. Jorgensen, T.; Hansen, T. K.; Becher, J. Tetrathiafulvalenes as Building-Blocks in Supramolecular Chemistry. *Chem. Soc. Rev.* **1994**, *23*, 41–51.
13. Lampard, C.; Murphy, J. A.; Lewis, N. Tetrathiafulvalene as a Catalyst for Radical-Polar Crossover Reactions. *J. Chem. Soc., Chem. Commun.* **1993**, 295–297.
14. Martín, N.; Sanchez, L.; Seoane, C.; Andreu, R.; Garín, J.; Orduna, J. Semiconducting Charge Transfer Complexes from [60]Fullerene-tetrathiafulvalene (C60-TTF) Systems. *Tetrahedron Lett.* **1996**, *37*, 5979–5982.
15. Nielsen, M. B.; Lomholt, C.; Becher, J. Tetrathiafulvalenes as Building Blocks in Supramolecular Chemistry II. *Chem. Soc. Rev.* **2000**, *29*, 153–164.
16. Oton, F.; Pfattner, R.; Oxtoby, N. S.; Mas-Torrent, M.; Wurst, K.; Fontrodona, X.; Olivier, Y.; Cornil, J.; Veciana, J.; Rovira, C. Benzodicarbomethoxytetrathiafulvalene Derivatives as Soluble Organic Semiconductors. *J. Org. Chem.* **2011**, *76*, 154–163.
17. Prato, M.; Maggini, M.; Giacometti, C.; Scorrano, G.; Sandona, G.; Farnia, G. Synthesis and Electrochemical Properties of Substituted Fulleropyrrolidines. *Tetrahedron* **1996**, *52*, 5221–5234.
18. Segura, J. L.; Martín, N. New Concepts in Tetrathiafulvalene Chemistry. *Angew. Chem., Int. Ed.* **2001**, *40*, 1372–1409.
19. Uchida, K.; Masuda, G.; Aoi, Y.; Nakayama, K.; Irie, M. Synthesis of Tetrathiafluvalene Derivatives with Photochromic Diarylethene Moieties. *Chem. Lett.* **1999**, *28*, 1071–1072.
20. Bryce, M. R. Functionalised Tetrathiafulvalenes: New Applications as Versatile π-Electron Systems in Materials Chemistry. *J. Mater. Chem.* **2000**, *10*, 589–598.
21. Simonsen, K. B.; Svenstrup, N.; Lau, J.; Simonsen, O.; Mork, P.; Kristensen, G. J.; Becher, J. Sequential Functionalisation of Bis-Protected Tetrathiafulvalene-Dithiolates. *Synthesis* **1996**, *1996*, 407–418.
22. Pittman, C. U.; Narita, M.; Liang, Y. F. Preparation and Reactions of Bifunctionalized Tetrathiafulvalenes. *J. Org. Chem.* **1976**, *41*, 2855–2860.
23. Qin, Y.-R.; Zhu, Q.-Y.; Huo, L.-B.; Shi, Z.; Bian, G.-Q.; Dai, J. Tetrathiafulvalene-Tetracarboxylate: An Intriguing Building Block with Versatility in Coordination Structures and Redox Properties. *Inorg. Chem.* **2010**, *49*, 7372–7381.
24. Lorcy, D.; Bellec, N.; Fourmigué, M.; Avarvari, N. Tetrathiafulvalene-Based Group XV Ligands: Synthesis, Coordination Chemistry and Radical Cation Salts. *Coord. Chem. Rev.* **2009**, *253*, 1398–1438.
25. Nguyen, T. L. A.; Demir-Cakan, R.; Devic, T.; Morcrette, M.; Ahnfeldt, T.; Auban-Senzier, P.; Stock, N.; Goncalves, A.-M.; Filinchuk, Y.; Tarascon, J.-M.; *et al.* 3-D Coordination Polymers Based on the Tetrathiafulvalene-Tetracarboxylate (TTF-TC) Derivative: Synthesis, Characterization, and Oxidation Issues. *Inorg. Chem.* **2010**, *49*, 7135–7143.
26. Nguyen, T. L. A.; Devic, T.; Mialane, P.; Rivière, E.; Sonnauer, A.; Stock, N.; Demir-Cakan, R.; Morcrette, M.; Livage, C.; Marrot, J.; *et al.* Reinvestigation of the MII (M = Ni, Co)/Tetrathiafulvalene-Tetracarboxylate System Using High-Throughput Methods: Isolation of a Molecular Complex and Its Single-Crystal-to-Single-Crystal Transformation to a Two-Dimensional Coordination Polymer. *Inorg. Chem.* **2010**, *49*, 10710–10717.
27. Majetich, S.; Carter, A.; McCullough, R. D.; Seth, J.; Belot, J. A. Connected CdSe Nanocrystallite Networks. *Z. Phys. D: At., Mol. Clusters* **1993**, *26*, 210–212.
28. Nakai, H.; Yoshihara, M.; Fujihara, H. New Electroactive Tetrathiafulvalene-Derivatized Gold Nanoparticles and their Remarkably Stable Nanoparticle Films on Electrodes. *Langmuir* **1999**, *15*, 8574–8576.
29. Ma, W.; Luther, J. M.; Zheng, H.; Wu, Y.; Alivisatos, A. P. Photovoltaic Devices Employing Ternary PbS_xSe_{1-x} Nanocrystals. *Nano Lett.* **2009**, *9*, 1699–1703.
30. Ravich, Y. I.; Efimova, B. A.; Tamarchenko, V. I. Scattering of Current Carriers and Transport Phenomena in Lead Chalcogenides. *Phys. Status Solidi B* **1971**, *43*, 11–33.
31. Tang, J.; Brzozowski, L.; Barkhouse, D. A. R.; Wang, X.; Debnath, R.; Wolowiec, R.; Palmiano, E.; Levina, L.; Pattantyus-Abraham, A. G.; Jamakosmanovic, D.; *et al.* Quantum Dot Photovoltaics in the Extreme Quantum Confinement Regime: The Surface-Chemical Origins of Exceptional Air- and Light-Stability. *ACS Nano* **2010**, *4*, 869–878.
32. Koh, W.; Saudari, S. R.; Fafarman, A. T.; Kagan, C. R.; Murray, C. B. Thiocyanate-Capped PbS Nanocubes: Ambipolar Transport Enables Quantum Dot Based Circuits on a Flexible Substrate. *Nano Lett.* **2011**, *11*, 4764–4767.
33. Kovalenko, M. V.; Scheele, M.; Talapin, D. V. Colloidal Nanocrystals with Molecular Metal Chalcogenide Surface Ligands. *Science* **2009**, *324*, 1417–1420.
34. Luther, J. M.; Law, M.; Song, Q.; Perkins, C. L.; Beard, M. C.; Nozik, A. J. Structural, Optical, and Electrical Properties of Self-Assembled Films of PbSe Nanocrystals Treated with 1,2-Ethanedithiol. *ACS Nano* **2008**, *2*, 271–280.
35. Nag, A.; Kovalenko, M. V.; Lee, J.-S.; Liu, W.; Spokoyny, B.; Talapin, D. V. Metal-Free Inorganic Ligands for Colloidal Nanocrystals: S^{2-}, HS^-, Se^{2-}, HSe^-, Te^{2-}, HTe^-, TeS_3^{2-}, OH^-, and NH_2^- as Surface Ligands. *J. Am. Chem. Soc.* **2011**, *133*, 10612–10620.
36. Tang, J.; Kemp, K. W.; Hoogland, S.; Jeong, K. S.; Liu, H.; Levina, L.; Furukawa, M.; Wang, X.; Debnath, R.; Cha, D.; *et al.* Colloidal-Quantum-Dot Photovoltaics Using Atomic-Ligand Passivation. *Nat. Mater.* **2011**, *10*, 765–771.
37. Zarghami, M. H.; Liu, Y.; Gibbs, M.; Gebremichael, E.; Webster, C.; Law, M. p-Type PbSe and PbS Quantum Dot Solids Prepared with Short-Chain Acids and Diacids. *ACS Nano* **2010**, *4*, 2475–2485.
38. Hines, M. A.; Scholes, G. D. Colloidal PbS Nanocrystals with Size-Tunable Near-Infrared Emission: Observation of Post-Synthesis Self-Narrowing of the Particle Size Distribution. *Adv. Mater.* **2003**, *15*, 1844–1849.
39. Axnanda, S.; Scheele, M.; Crumlin, E. J.; Mao, B.; Chang, R.; Rani, S.; Faiz, M.; Wang, S.; Alivisatos, A. P.; Liu, Z. Direct Work Function Measurement by Gas Phase Photoelectron Spectroscopy and Its Application on PbS Nanoparticles. *Nano Lett.* **2013**, *13*, 6176–6182.
40. Mercier, N.; Giffard, M.; Pilet, G.; Allain, M.; Hudhomme, P.; Mabon, G.; Levillain, E.; Gorgues, A.; Riou, A. $(TTF)_2[TTF-(CO_2H)_2(CO_2)_2]$: a Wholly TTF Material Containing TTF Radical Cations and TTF Derived Anions. *Chem. Commun.* **2001**, 2722–2723.
41. Zhu, Q.-Y.; Han, Q.-H.; Shao, M.-Y.; Gu, J.; Shi, Z.; Dai, J. Supramolecular and Redox Chemistry of Tetrathiafulvalene-Monocarboxylic Acid with Hydrogen-Bonded Pyridine and Bipyridine Molecules. *J. Phys. Chem. B* **2012**, *116*, 4239–4247.
42. Hedin, L. New Method for Calculating the One-Particle Green's Function with Application to the Electron-Gas Problem. *Phys. Rev.* **1965**, *139*, A796–A823.
43. Heyd, J.; Scuseria, G. E.; Ernzerhof, M. Hybrid Functionals Based on a Screened Coulomb Potential. *J. Chem. Phys.* **2003**, *118*, 8207–8215.

44. Kresse, G.; Hafner, J. Ab Initio Molecular Dynamics for Liquid Metals. *Phys. Rev. B* **1993**, *47*, 558–561.
45. Kresse, G.; Joubert, D. From Ultrasoft Pseudopotentials to the Projector Augmented-Wave Method. *Phys. Rev. B* **1999**, *59*, 1758–1775.
46. Shishkin, M.; Kresse, G. Implementation and Performance of the Frequency-Dependent GW Method within the PAW Framework. *Phys. Rev. B* **2006**, *74*, 035101–035113.
47. Gai, Y.; Peng, H.; Li, J. Electronic Properties of Nonstoichiometric PbSe Quantum Dots from First Principles. *J. Phys. Chem. C* **2009**, *113*, 21506–21511.
48. Wang, L.-W. Charging Effects in a CdSe Nanotetrapod. *J. Phys. Chem. B* **2005**, *109*, 23330–23335.
49. Wang, L.-W.; Zhao, Z.; Meza, J. Linear-Scaling Three-dimensional Fragment Method for Large-Scale Electronic Structure Calculations. *Phys. Rev. B* **2008**, *77*, 165113–5.
50. Zhao, Z.; Meza, J.; Wang, L.-W. A Divide-and-Conquer Linear Scaling Three-Dimensional Fragment Method for Large Scale Electronic Structure Calculations. *J. Phys.: Condens. Matter* **2008**, *20*, 294203–294208.
51. Chourou, S. T.; Sarje, A.; Li, X. S.; Chan, E. R.; Hexemer, A. HipGISAXS: a High-Performance Computing Code for Simulating Grazing-Incidence X-ray Scattering Data. *J. Appl. Crystallogr.* **2013**, *46*, 1781–1795.
52. Choi, J. J.; Bealing, C. R.; Bian, K.; Hughes, K. J.; Zhang, W.; Smilgies, D.-M.; Hennig, R. G.; Engstrom, J. R.; Hanrath, T. Controlling Nanocrystal Superlattice Symmetry and Shape-Anisotropic Interactions through Variable Ligand Surface Coverage. *J. Am. Chem. Soc.* **2011**, *133*, 3131–3138.
53. Law, M.; Luther, J. M.; Song, Q.; Hughes, B. K.; Perkins, C. L.; Nozik, A. J. Structural, Optical, and Electrical Properties of PbSe Nanocrystal Solids Treated Thermally or with Simple Amines. *J. Am. Chem. Soc.* **2008**, *130*, 5974–5985.
54. Talapin, D. V.; Murray, C. B. PbSe Nanocrystal Solids for n- and p-Channel Thin Film Field-Effect Transistors. *Science* **2005**, *310*, 86–89.
55. Ehrler, B.; Walker, B. J.; Böhm, M. L.; Wilson, M. W. B.; Vaynzof, Y.; Friend, R. H.; Greenham, N. C. *In Situ* Measurement of Exciton Energy in Hybrid Singlet-Fission Solar Cells. *Nat. Commun.* **2012**, *3*, 1019–6.
56. Jasieniak, J.; Califano, M.; Watkins, S. E. Size-Dependent Valence and Conduction Band-Edge Energies of Semiconductor Nanocrystals. *ACS Nano* **2011**, *5*, 5888–5902.
57. Timp, B. A.; Zhu, X.-Y. Electronic Energy Alignment at the PbSe Quantum Dots/ZnO(10−10) Interface. *Surf. Sci.* **2010**, *604*, 1335–1341.
58. Hyun, B.-R.; Zhong, Y.-W.; Bartnik, A. C.; Sun, L.; Abruna, H. D.; Wise, F. W.; Goodreau, J. D.; Matthews, J. R.; Leslie, T. M.; Borrelli, N. F. Electron Injection from Colloidal PbS Quantum Dots into Titanium Dioxide Nanoparticles. *ACS Nano* **2008**, *2*, 2206–2212.
59. Fourmigué, M.; Batail, P. Activation of Hydrogen- and Halogen-Bonding Interactions in Tetrathiafulvalene-Based Crystalline Molecular Conductors. *Chem. Rev.* **2004**, *104*, 5379–5418.
60. Shevchenko, E. V.; Talapin, D. V.; Kotov, N. A.; O'Brien, S.; Murray, C. B. Structural Diversity in Binary Nanoparticle Superlattices. *Nature* **2006**, *439*, 55–59.
61. Wang, Z.; Schliehe, C.; Bian, K.; Dale, D.; Bassett, W. A.; Hanrath, T.; Klinke, C.; Weller, H. Correlating Superlattice Polymorphs to Internanoparticle Distance, Packing Density, and Surface Lattice in Assemblies of PbS Nanoparticles. *Nano Lett.* **2013**, *13*, 1303–1311.
62. Leschkies, K. S.; Kang, M. S.; Aydil, E. S.; Norris, D. J. Influence of Atmospheric Gases on the Electrical Properties of PbSe Quantum-Dot Films. *J. Phys. Chem. C* **2010**, *114*, 9988–9996.
63. Liu, Y.; Gibbs, M.; Puthussery, J.; Gaik, S.; Ihly, R.; Hillhouse, H. W.; Law, M. Dependence of Carrier Mobility on Nanocrystal Size and Ligand Length in PbSe Nanocrystal Solids. *Nano Lett.* **2010**, *10*, 1960–1969.
64. Schroeder, J. H. *Herstellung Und Charakterisierung von Schichtsystemen Aus Gold-Nanopartikeln*, University of Hamburg, 2012.
65. Liu, Y.; Tolentino, J.; Gibbs, M.; Ihly, R.; Perkins, C. L.; Liu, Y.; Crawford, N.; Hemminger, J. C.; Law, M. PbSe Quantum Dot Field-Effect Transistors with Air-Stable Electron Mobilities above 7 $cm^2 V^{-1} s^{-1}$. *Nano Lett.* **2013**, *13*, 1578–1587.